



Upgrading structural conjugation in covalent organic framework with spatial dual sites enables boosting solar-to-H₂O₂-to-•OH for environmental remediation

Jinpeng Zhang^a, Guocheng Huang^{a,*}, Qiaoshan Chen^a, Ling Wu^b, Liuyi Li^c, Jinhong Bi^{a,b,**}

^a Department of Environmental Science and Engineering, Fuzhou University, Fuzhou 350108, PR China

^b State Key Laboratory of Photocatalysis on Energy and Environment, Fuzhou University, Fuzhou 350108, PR China

^c Key Laboratory of Eco-materials Advanced Technology, College of Materials Science and Engineering, Fuzhou University, Fuzhou 350108, PR China

ARTICLE INFO

Keywords:

Covalent organic frameworks

Photocatalysis

Spatial dual sites

H₂O₂ activation

Hydroxyl radicals

ABSTRACT

Designing photocatalysts with well-defined structure-function relationships is imperative for propelling the progression of desired photocatalytic oxidation. Herein, the efficient conversion of solar energy to H₂O₂ and subsequently to hydroxyl radicals (•OH) is achieved through a synergistic interplay between olefin linkage (-C=C-) and spatially separated benzene-triazine dual reaction sites within covalent organic frameworks (COFs). The upgraded -C=C- can increase the conjugation degree of COFs, which establishes an expanded superstructure for boosting charge separation/transfer and stability. This precise modulation renders more opportunities for the hot electrons to migrate to the benzene site for solar-to-H₂O₂ generation, and to the triazine site for H₂O₂-to-•OH, separately. The optimized •OH generation pathway enables remarkable oxidation performances against recalcitrant organic pollutants, and pathogenic microorganisms under visible light irradiation. This work provides new insights for tuning the synergistic interactions of various building blocks within the COFs for the selective generation of highly reactive •OH for environmental remediation.

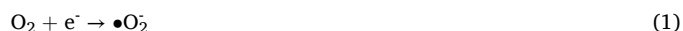
1. Introduction

Hydroxyl radical (•OH) holds great significance in the realm of environmental remediation, primarily due to its exceptional oxidizing capabilities [1]. Currently, prominent methods for generating •OH encompass the Fenton reaction and UV/H₂O₂ processes [2]. Nonetheless, the Fenton reaction is encumbered by certain limitations, including potential toxicity of iron, secondary sludge formation [3], while UV/H₂O₂ processes are associated with elevated energy consumption [4]. Notably, both methods require the addition of H₂O₂.

An environmentally benign alternative involves the utilization of semiconductor-based photocatalysis to generate •OH using solar energy [5]. Nonetheless, the production of •OH through direct water oxidation by holes (h⁺) is hindered by the high electrode potential requirement (e.g. E_{•OH/OH} = 1.99 V, E_{•OH/H₂O} = 2.27 V vs. NHE at pH = 7), precluding most photocatalysts capable of absorbing visible light [6–8].

A fascinate alternative for photocatalytic •OH production entails the stepwise oxygen reduction reaction (ORR) photosynthesis of H₂O₂

followed by its *in-situ* photodecomposition as described in Eqs. (1)–(3) [9–12].



However, knowledge regarding the reduction specificity of the conduction band-electrons (CB-e⁻) between •O₂⁻ vs. H₂O₂ remains ambiguous in the field of photocatalysis [13]. On one hand, under conditions where pH is less than 9.9, the likelihood of H₂O₂ yield through the ORR (Eqs. (1) and (2)) surpasses the reduction of H₂O₂ to •OH (Eq. (3)), as the reduction potential of •O₂⁻ is slightly more positive than that of H₂O₂ [14]. Hence, H₂O₂ has been commonly identified as the major end-product originated from the CB-e⁻ rather than the •OH [15]. On the other hand, the CB-e⁻ reduction propensities over •O₂⁻ vs. H₂O₂ can undergo substantial variations depending upon coordination and electronic structures of reaction site, given that the actual reduction

* Corresponding author.

** Corresponding author at: Department of Environmental Science and Engineering, Fuzhou University, Fuzhou 350108, PR China.

E-mail addresses: huanggch@fzu.edu.cn, syuhgc@gmail.com (G. Huang), bijinhong@fzu.edu.cn (J. Bi).

<https://doi.org/10.1016/j.apcatb.2024.124216>

Received 19 March 2024; Received in revised form 16 May 2024; Accepted 17 May 2024

Available online 18 May 2024

0926-3373/© 2024 Elsevier B.V. All rights are reserved, including those for text and data mining, AI training, and similar technologies.

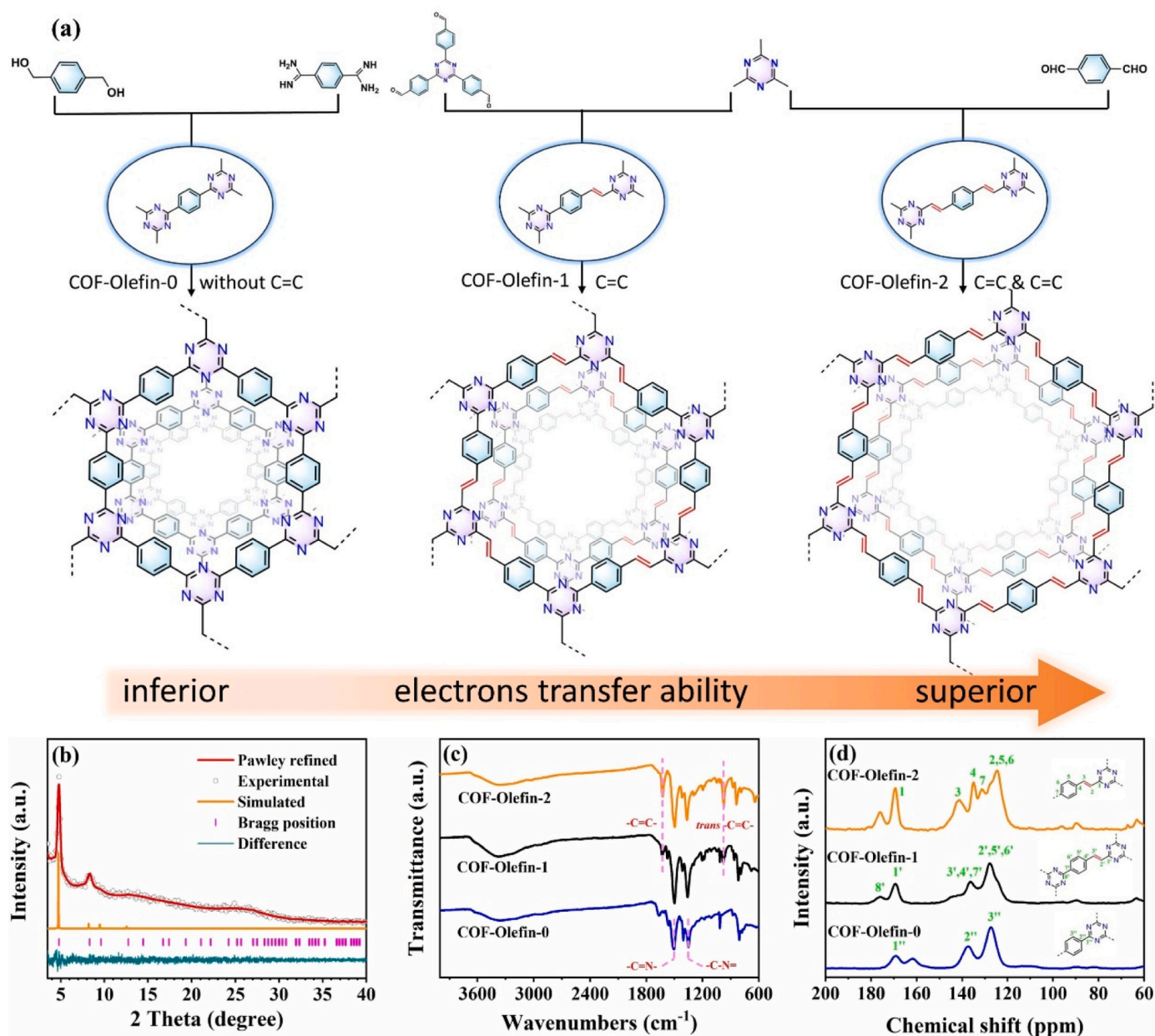


Fig. 1. (a) Illustration of synthetic procedures for COF-Olefin-0, COF-Olefin-1 and COF-Olefin-2; (b) PXRD patterns of COF-Olefin-2; (c) FT-IR and (d) ¹³C CP/MAS ssNMR spectra of COF-Olefin-2, COF-Olefin-1 and COF-Olefin-0.

processes occur at specific substrate-adsorbed state [16]. Thus, rationally design photocatalysts with spatially separated dual reaction sites that accurately identify and activate O₂/H₂O₂, to achieve solar-to-H₂O₂-to-•OH process for environmental remediation.

Recently, covalent organic frameworks (COFs) have emerged as a new option for developing photocatalytic materials with well-defined and ordered structures [17,18]. COFs are crystalline porous organic materials formed through covalent bonds between organic building blocks. Their molecular-level design and synthesis afford precise control of specific and multiple catalytic units, thereby enabling the elucidation of the intricate structure-function relationship [19,20]. The benzene- and triazine-unit are ubiquitous constituents in constructing COF, owing to their inherently planar and rigid structures. Additionally, these units facilitate π - π stacking interactions, thereby enhancing the overall stability and porosity of the resultant framework [21,22]. Previous studies have indicated that the benzene unit in COF can function as electron acceptor, thereby expediting the prompt activation and conversion of O₂

into H₂O₂ [23]. Meanwhile, the triazine-unit can further act as an active center for the *in-situ* decomposition of H₂O₂ into •OH [24]. Consequently, it is reasonable to postulate that the incorporation of a benzene-triazine dual site within COFs to achieve solar-to-H₂O₂-to-•OH process.

In addition, there is still a pressing need to enhance the efficiency of photogenerated carrier separation of COFs. Various strategies, including heteroatom doping [25,26], functional group modification [27,28], heterojunction formation [29,30], and incorporation of donor-acceptor structures [31,32] have been postulated. While strategies pertain to the linkage chemistry and building blocks are scarce. Generally, olefin linkage (-CH=CH-) can serve as π -bridges to establish connections between the spatially separated building blocks, thereby extending the x-y plane π conjugation. This extended conjugation allows for the efficient delocalization of electrons across a larger area of the COF, enhancing the overall conjugation degree. Consequently, the likelihood of charge carriers recombination is reduced. Therefore, the insertion of

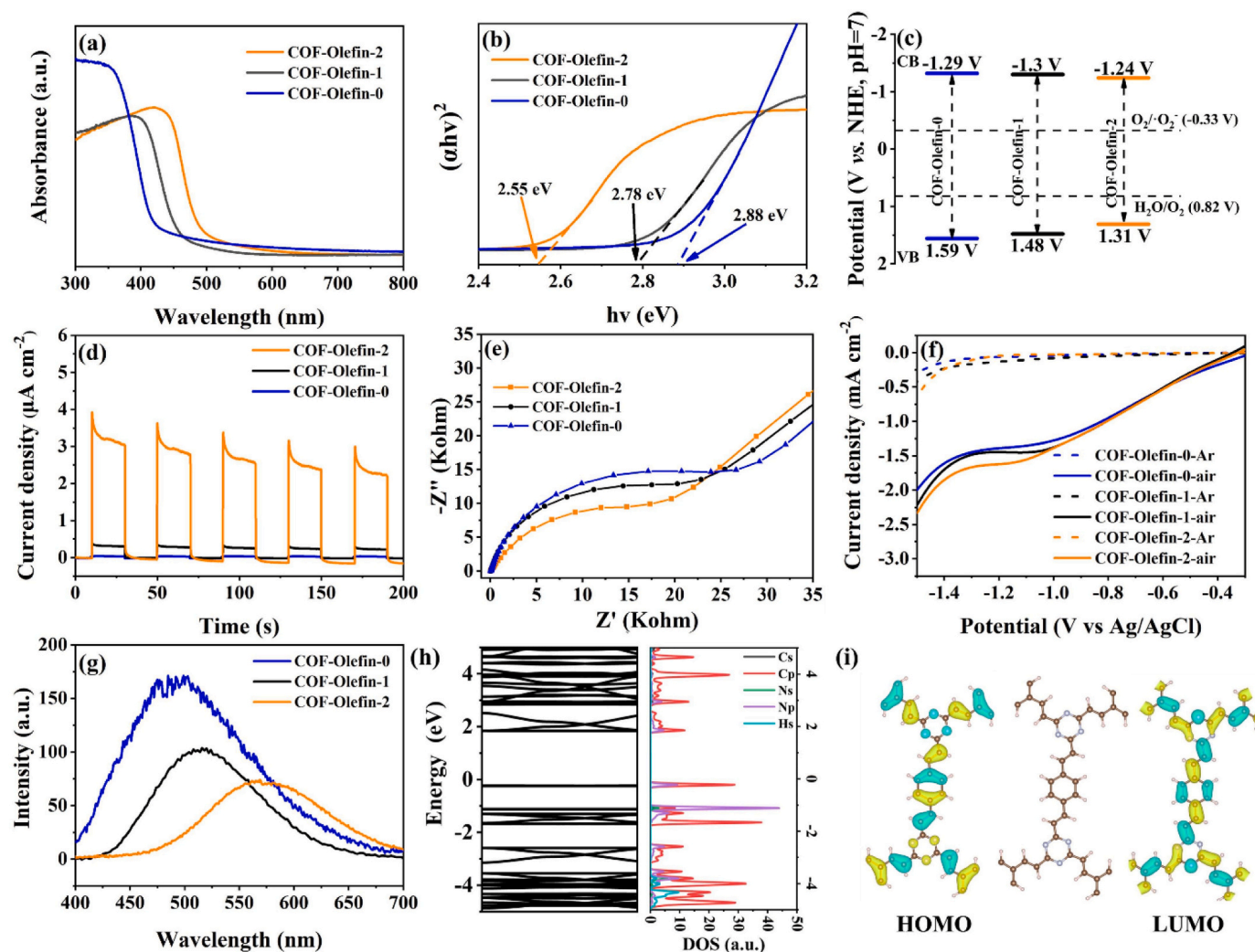


Fig. 2. (a) Solid-state ultraviolet/visible diffuse reflectance spectra; (b) Tauc plots; (c) Band alignment; (d) Transient photocurrent response; (e) Electrochemical impedance spectroscopy Nyquist plots; (f) Linear sweep voltammograms; (g) Photoluminescence spectra for COFs; (h) Electronic properties of COF-Olefin-2 using DFT calculations and corresponding density of states; (i) DFT-optimized molecular orbital plots of COF-Olefin-2.

conjugated linkage components in COFs holds promise for the design of highly efficient photocatalysts [33–36].

In this work, a benzene-triazine dual site COFs linked with varying amounts of $-\text{CH}=\text{CH}-$ (0, 1, 2) were fabricated via ion-thermal and solve-thermal methods. By introducing $-\text{CH}=\text{CH}-$, the $\bullet\text{OH}$ generation pathway was optimized to achieve remarkable solar-to- H_2O_2 -to- $\bullet\text{OH}$ at a low oxidation potential, which contributes to outstanding efficacy in the photodegradation of organic pollutant and pathogenic microorganisms. Experiments and DFT calculations demonstrate that the $-\text{CH}=\text{CH}-$ acted as π -bridges to upgrading the whole conjugation level in COFs but also modulated the coordination and electronic structures of benzene-triazine dual sites for cascading solar-to- H_2O_2 and H_2O_2 -to- $\bullet\text{OH}$, respectively. This photocatalytic oxidation system is entirely metal-free and energy-renewable, thus paving a sustainable pathway for on-site environmental remediation.

2. Experimental

The synthesis procedure as depicted in Fig. 1a, COF-Olefin-1 and COF-Olefin-2 were synthesized using a solvothermal method. 2,4,6-Tri-methyl-1,3,5-triazine (0.25 mmol), 1,4-diformylbenzene (0.75 mmol) and potassium hydroxide (1.5 mmol) were dissolved in a mixed solvent containing 7 mL n-butanol and 3 mL 1,2-dichlorobenzene. The mixture was heated at 393 K and reacted for 72 h. After cooling to room

temperature, the samples were washed and precipitated with methanol, tetrahydrofuran, acetone and dichloromethane, and dried under vacuum at 393 K for 12 h to obtain the sample of COF-Olefin-2. COF-Olefin-1 was obtained by replacing the precursor 1,4-dimethylbenzene with 1,3,5-tri(4-formylphenyl) triazine.

COF-Olefin-0 was synthesized through an ion thermal method. A mixture containing 1,4-benzenedimethanol (0.5 mmol), terephthalimidamide dihydrochloride (1.0 mmol), caesium carbonate (1.1 mmol), and dimethyl sulfoxide (15 mL) was heated at 373 K for 24 h and then at 453 K for 36 h. The precipitate was washed with 1 M dilute hydrochloric acid, water, ethanol, and tetrahydrofuran. Finally, the filtered solids were freeze-dried for 24 h, and the power obtained was denoted as COF-Olefin-0 [37,38].

Detailed experimental sections of chemicals, characterizations, photocatalytic experiments, and computational details were illustrated in the Supporting information.

3. Results and discussion

3.1. Structural characterizations

The pore characteristics of the three COFs were determined by measuring the nitrogen adsorption isotherms at 77 K (Fig. S1). The adsorption isotherms of both COFs expressed a steep absorption in the

low-pressure range, which is consistent with the type I sorption isotherm and indicative of microporosity [39]. With increasing gas pressure, the COF pores expanded, resulting in a hysteresis in the isotherm. The calculated Brunauer-Emmett-Teller (BET) surface areas for COF-Olefin-0, COF-Olefin-1, and COF-Olefin-2 were determined to be 489.56, 553.15 and 611.75 m² g⁻¹, respectively, as presented in Table S1.

The crystalline phase structure of the COFs was comprehensively characterized using powder X-ray diffraction (PXRD) experiments along with theoretical simulations (Fig. 1b and S2). The PXRD patterns exhibited distinct diffraction peaks at $2\theta = 7.3^\circ$, 12.2° , 14.7° , and 26.2° for COF-Olefin-0, $2\theta = 5.7^\circ$, 9.8° , 11.9° , 15.0° and 26.3° for COF-Olefin-1 and $2\theta = 4.7^\circ$, 8.3° , 9.5° , 12.7° and 26.6° for COF-Olefin-2. The eclipsed AA layer stacking model was built using the Material Studio software package, and the experimental PXRD patterns match this model with a negligible difference. Meanwhile, the results of Pawley refinement accurately match the observed PXRD patterns. Scanning electron microscopy (SEM) and transmission electron microscopy (TEM) observation in Fig. S3a–f reveal that COF-Olefin-1 has a flocculent stacking morphology, COF-Olefin-2 has a nanoribbon interlaced structure, while COF-Olefin-0 has irregular layered accumulation. Fast Fourier transform (FFT) and inverse fast Fourier transform (IFFT) analyses were performed using TEM images at a higher magnification (Fig. S3g–i) [40]. Notably, the FFT and IFFT spectra were not observed for COF-Olefin-0, which can be attributed to its poor crystallinity [41]. Meanwhile, the diffraction points corresponding to the (1 0 0) planes of COF-1 and COF-2 were identified, with their respective interplanar distances determined as 1.8 and 1.9 nm. It is worth noting that the utilization of a high beam energy during high-resolution TEM (HRTEM) observations could result in the loss of remotely ordered information, thus impeding the direct observation of the crystal lattice in HRTEM images (Fig. S3j–l) [42].

The fourier transform infrared (FT-IR) and solid-state ¹³C cross-polarization magic angle spinning nuclear magnetic resonance (CP/MAS ssNMR) spectroscopy were conducted to ascertain their chemical structures. The FT-IR spectrum of COF-Olefin-0 (Fig. 1c) displayed characteristic peaks at 1517 cm⁻¹ and 1360 cm⁻¹, indicating the successful formation of the triazine framework. These characteristic peaks were also observed in COF-Olefin-1 and COF-Olefin-2. Notably, the peaks at 1626 cm⁻¹ and 974 cm⁻¹ attributed to stretching vibration peaks of newly formed -C=C- moieties in trans-configuration were indicative of the existence of -CH=CH- [43]. Additionally, the absorption peak at approximately 3400 cm⁻¹ was attributed to the O-H stretching vibration caused by adsorbed H₂O in the COFs [44]. In ssNMR spectra (Fig. 1d), COF-Olefin-2 exhibited five prominent resonances at 170, 140, 135, 130, and 125 ppm, corresponding to the carbon atoms of the triazine moiety (labeled 1), the carbon atoms of the olefin group (labeled 3), the olefin-linked phenyl carbon (labeled 4), the phenyl linked carbon (labeled 7), and alkene carbon (labeled 2) overlapped with the hydrogen-bonded aromatic carbon (labeled 5 and 6), respectively [28]. COF-Olefin-1 exhibited resonances at 120–140 ppm assigned to the phenyl and -C=C- carbons, along with resonances at 170 ppm and 176 ppm attributed to the triazine core [45]. In COF-Olefin-0, resonances at 127 ppm and 137 ppm were assigned to the phenyl carbons, while the resonance at 170 ppm was attributed to the carbon signal of the triazine unit [46]. Collectively, these results confirm the structural integrity of the three COFs.

3.2. Band structures

The optical properties of the three COFs were evaluated using solid-state ultraviolet/visible diffuse reflectance spectra (UV-vis DRS). The results, shown in Fig. 2a, demonstrated excellent absorption ability of all COFs in the visible region [47]. Importantly, the absorption of the COFs exhibited a significant red-shift with an increase in -CH=CH- content, indicating that the extended π -conjugated structure enhanced the

light-harvesting ability in the visible region. The optical band gaps were determined using the Kubelka-Munk equation and plotted in the Tauc plot pattern (Fig. 2b). COF-Olefin-2 exhibited the narrowest band gap, measuring 2.55 eV, followed by COF-Olefin-1 with a band gap of 2.78 eV, while COF-Olefin-0 had the largest band gap of 2.88 eV. Furthermore, the valence band-X-ray photoelectron spectroscopy (VB-XPS) (Fig. S4) was measured to obtain the valence band potential ($E_{VB, XPS}$). The corresponding $E_{VB, XPS}$ of COF-Olefin-0, COF-Olefin-1, and COF-Olefin-2 were estimated to be 1.53, 1.42, and 1.25 eV, respectively. Then, the $E_{VB, NHE}$ of COF-Olefin-0, COF-Olefin-1, and COF-Olefin-2 were calculated as 1.59, 1.48, and 1.31 V vs. NHE through the formula: $E_{VB, NHE} = \phi + E_{VB, XPS} - 4.44$, where ϕ is the work function of the instrument (4.5 eV) [48]. In addition, the conduction potentials of COF-Olefin-0, COF-Olefin-1, and COF-Olefin-2 were determined to be -1.29, -1.3 and -1.24 V, respectively, based on the formula $E_g = E_{VB} - E_{CB}$. Hence, the band structure alignments of the three COFs can be obtained as illustrated in Fig. 2c.

3.3. Photoelectrochemical properties

A significant photocurrent response (Fig. 2d) of COF-Olefin-2 was observed, signifying that the COF-Olefin-2 has great potential for constructing a robust photocatalytic system [49]. In the electrochemical impedance spectroscopy (EIS) Nyquist plot (Fig. 2e), COF-Olefin-2 exhibited the smallest semicircle, indicating the lowest charge transfer resistance among the COFs [50]. The linear sweep voltammogram (LSV) was used to evaluate the photo-electrochemical performance of the three COFs under different conditions (Fig. 2f). COF-Olefin-2 displayed the highest current density, reaching 2.7 mA cm⁻² at -1.5 V vs. Ag/AgCl, demonstrating that the introduction of -C=C- efficiently promotes the photocatalytic oxygen reduction reaction [51]. The photoluminescence (PL) intensity for COF-Olefin-2 (Fig. 2g) was significantly lower compared to COF-Olefin-1 and COF-Olefin-0, indicating that the excited state electrons of COF-Olefin-0 and COF-Olefin-1 tend to combine with holes and release energy in the form of photons [52]. Additionally, with an increase in the number of -C=C- moieties, the COFs exhibited a red shift in the maximum emission wavelength, attributed to the extended π -conjugation [53]. The time-resolved photoluminescence (TRPL) results showed that the average lifetimes of COF-Olefin-0, COF-Olefin-1, and COF-Olefin-2 were 0.53, 0.63, and 4.80 ns, respectively (Fig. S5). The lower fluorescence intensities and longer excited-state lifetimes suggest that the introduction of -C=C- promotes charge separation [54].

3.4. Electronic structures calculated by Density Functional Theory

The electronic structures of the COFs were further investigated using Density Functional Theory (DFT) calculations. In the projected density of states (PDOS) profile (Fig. 2h and S6) [55], it was observed that the valence band primarily originates from the 2p orbitals of the carbon (C) and nitrogen (N) atoms, while the conduction band is associated with the C 2p orbital. Binding resonances near the Fermi level were also evident. These results indicate that the excited electrons in the COFs mainly arise from the superior π -delocalization from the C 2p orbital, followed by the N 2p orbital. The trend of band gap variations determined by DFT calculations aligns with the experimental UV-vis DRS results. These calculated results confirm semiconductor nature of the three COFs. Moreover, calculations of the charge density distribution of the lowest unoccupied molecular orbital (LUMO) and the highest occupied molecular orbital (HOMO) were performed to analyze the electron distribution (Fig. 2i and S7). The distribution of electrons in the building blocks of the three COFs differed. COF-Olefin-2 exhibited a stronger electron distribution uniformity in its LUMO and HOMO compared to the other COFs. This demonstrates that the extended π -conjugated structure facilitates the transfer of delocalized π -electrons [56].

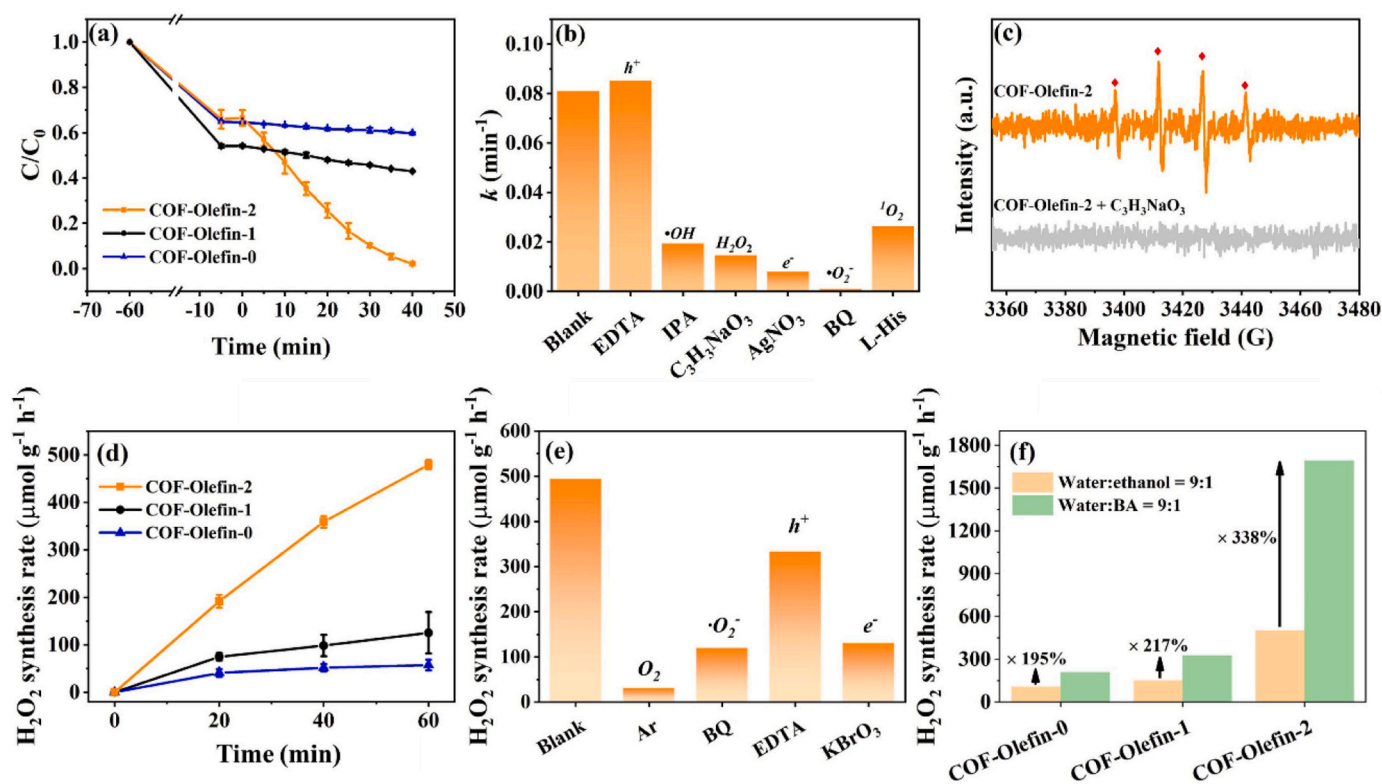


Fig. 3. (a) Photocatalytic degradation of 20 ppm CBZ over COFs; (b) Quenching tests on CBZ degradation by COF-Olefin-2; (c) ESR spectrum after trapping H_2O_2 in COF-Olefin-2 system; (d) H_2O_2 synthesis rate of COFs; (e) Quenching tests on H_2O_2 synthesis by COF-Olefin-2; (f) Photoactivity of the COFs for H_2O_2 production after 40 min of irradiation in different systems: water: ethanol = 9:1 (50 mL, 5 mg COF; one-phase system), water: BA = 9:1 (50 mL, 5 mg COF; two-phase system). Bars represent the standard deviation of three replicates in this work.

3.5. Catalytic performances

The photocatalytic activities of the COFs were evaluated by comparing the degradation of carbamazepine (CBZ) under visible light. Fig. 3a shows that COF-Olefin-2 exhibits the highest activity, consistent with the abovementioned electronic properties. It is generally recognized that the catalysts with larger pore sizes tend to have better degradation efficiency due to their ability to adsorb pollutants more easily and promote subsequent degradation [57]. However, during the dark adsorption stage (Fig. 3a: -60 min to 0 min), COF-Olefin-2, with the largest pore size, did not exhibit the best CBZ adsorption capacity. This suggests that the improvement in photocatalytic performance is not solely due to changes in adsorption capacity caused by pore size, but rather is a result of excellent photoelectric characteristics. The pseudo-first-order model (Fig. S8) was used to investigate the kinetics of CBZ degradation. The degradation rate constant (k) of COF-Olefin-2 was found to be $0.0811\ min^{-1}$, significantly higher than that of COF-Olefin-1 ($0.006\ min^{-1}$) and COF-Olefin-0 ($0.002\ min^{-1}$).

To verify the recyclability of COF-Olefin-2, four cycles of experiments were conducted. As shown in Fig. S9, The degradation efficiency remained above 84 % after four cycles, and no changes were observed in the XRD, FTIR, and ^{13}C NMR spectra of COF-Olefin-2 (Fig. S10) of COF-Olefin-2. Analysis of the elements in COF-Olefin-2 before and after the reaction using energy dispersive X-ray (EDX) (Fig. S11) demonstrated that the content of C and N elements did not change significantly, indicating the structural integrity of COF-Olefin-2 after the reaction. The significant increase of O element after the reaction may be caused by the adsorption of O_2 and H_2O by COF-Olefin 2 during the reaction. In addition, the composition of the solution in pure water system before and after light irradiation was analyzed by 1H NMR. It can be seen from Fig. S12, only the characteristic peak representing H_2O was found except for d6-DMSO, indicating that COF-Olefin 2 did not decompose after the

reaction. These results indicate that COF-Olefin-2 maintains structure integrity. The total organic carbon (TOC) removal efficiency (Fig. S13) exhibited a similar trend to CBZ degradation efficiency in different systems after 40 min reaction. Four different pharmaceutical and personal care products (PPCPs), including tetracycline (TC), ciprofloxacin (CIP), sulfafurazole (SIZ) and diclofenac sodium (DF) degradation experiments (Fig. S14) were conducted to test the universality of COF-Olefin-2. The degradation efficiency for all the mentioned PPCPs can reach 99 % in 40 min. Compared with other reported photocatalysts for degrading PPCPs (Table S2), COF-Olefin-2 has the superior photocatalytic degradation efficiency. Photocatalytic bacterial disinfection experiments (Fig. S15) were also conducted, showing that COF-Olefin-2 was able to completely inactivate $\sim 7\ log\ CFU\ mL^{-1}$ of *Escherichia coli* (*E. coli*) and *Staphylococcus aureus* (*S. aureus*), indicating its disinfection capacity. The corresponding flat colony pictures are shown in Fig. S16. The excellent universality of COF-Olefin-2 enables it to handle complex situations for environment remediation. In addition, experiments on CBZ degradation under sunlight were conducted (Fig. S17), and COF-Olefin-2 was able to achieve complete degradation of CBZ within 80 min. These results highlight the great environmental potential of COF-Olefin-2 for effective oxidation using sunlight as an energy source.

3.6. Mechanism of photodegradation

The quenching experiments and the corresponding pseudo-first-order fitting (Fig. 3b and S18) were conducted to further distinguish the contribution of all the reactive oxygen species (ROSs), in which 1,4-benzoquinone (BQ), silver nitrate ($AgNO_3$), L-histidine (L-His), ethylenediaminetetraacetic acid disodium salt (EDTA), isopropanol (IPA), and sodium pyruvate ($C_3H_3NaO_3$) were treated as $\cdot O_2^-$, e^- , 1O_2 , h^+ , $\cdot OH$, and H_2O_2 scavengers, respectively [58]. When BQ, $AgNO_3$, $C_3H_3NaO_3$ and L-His were added, the inhibition rates reached 98.68%, 91.10%,

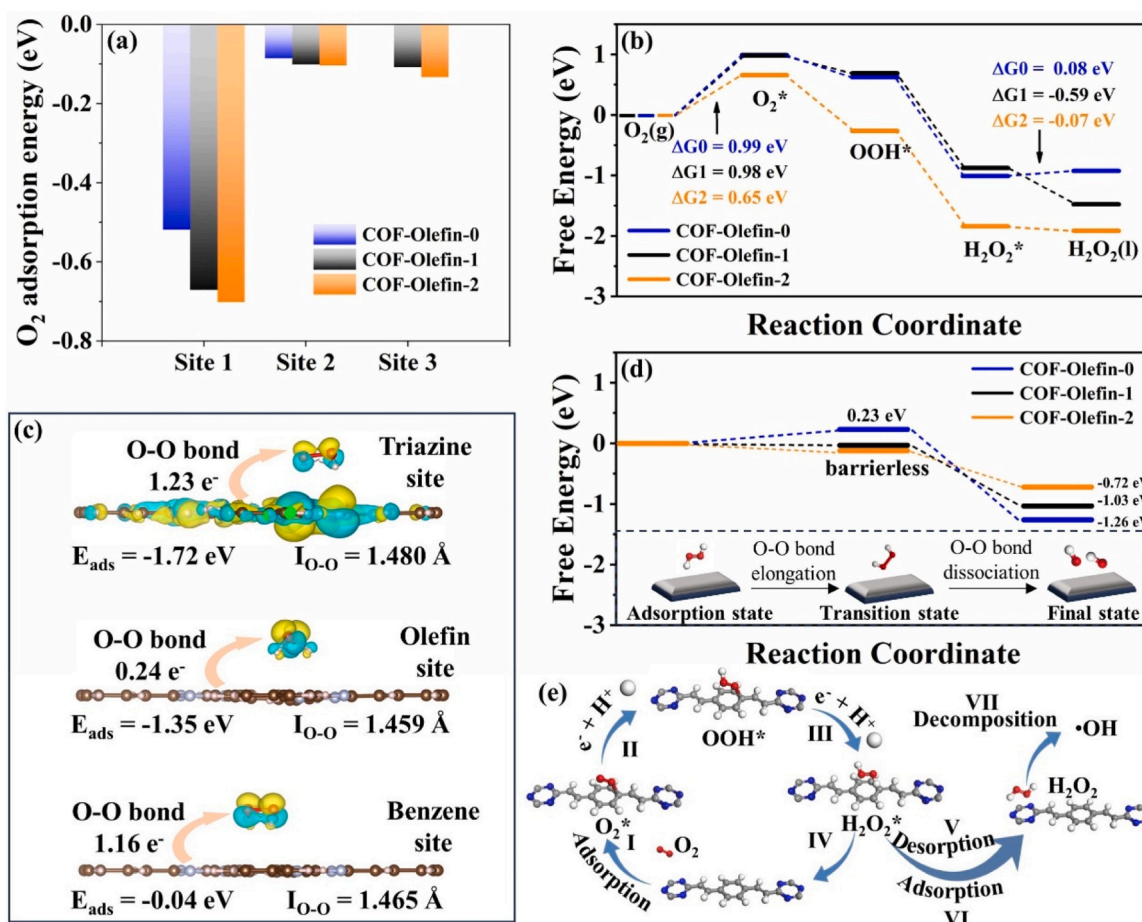


Fig. 4. (a) The calculated adsorption energy of O₂ on different sites of COFs. In COF-Olefin-2, site 1 is the benzene, site 2 is the triazine, and site 3 is the olefin linkage; (b) Free-energy diagrams for the reduction of O₂ to H₂O₂ on COFs; (c) Adsorption energy, charge density difference and electron transfer (Bader analysis) of H₂O₂ adsorbed at different sites of COF-Olefin-2; (d) Transition state energy of H₂O₂ reductive activation to •OH; (e) Key steps of •OH production by COF-Olefin-2.

83.45% and 53.15%, respectively, indicating that e⁻ derived •O₂, H₂O₂, •OH and ¹O₂ played crucial roles in the COF-Olefin-2 system. The increase in degradation rate after trapping of h⁺ may be due to the EDTA acting as a sacrificial agent, reducing the e⁻-h⁺ recombination. This postulation was further verified by comparing the PL spectra of COF-Olefin-2 with and without the presence of EDTA. As shown in Fig. S19, when EDTA was added, the fluorescence intensity was decreased, indicating that EDTA could quench the h⁺ and reduce the recombination of e⁻-h⁺, thereby improving the photocatalytic performance. In addition, H₂O₂ solution at concentration equals to COF-Olefin-2 yield at 40 min was applied for CBZ degradation (Fig. S20). Results show that the H₂O₂ alone cannot damage the stable CBZ molecule due to its weak oxidation ability. This conflicts with quenching experiments, implying the contributive role of H₂O₂ could be due to its conversion to other strong ROSs such as •OH. The electron spin response (ESR) spectroscopy was performed using 5,5-dimethyl-1-pyrroline N-oxide (DMPO) as spin trapping agents to further determine the existence of •OH (Fig. 3c) [59,60]. Under visible light irradiation, COF-Olefin-2 system showed apparently DMPO-•OH characteristic peaks, and the DMPO-•OH signal disappeared after the addition of H₂O₂ scavenger (C₃H₃NaO₃). Noted that the VB of COF-Olefin-2 does not positive enough for •OH production from water oxidation. Collectively, these results manifest that the •OH in the COF-Olefin-2 system was generated by H₂O₂ activation via Fenton-like reaction at low oxidation potential. To further clarify the role of •O₂, a double-scavengers experiment using IPA and L-His were conducted. As shown in Fig. S21, when •OH and ¹O₂ were both quenched, the inhibition rate was the lowest, indicating that remaining •O₂ alone had the lowest ability to

degrade CBZ among •O₂, •OH and ¹O₂. Therefore, the effective participation of •O₂ in the quenching experiments could be attributed to its role as precursor for generation of H₂O₂ and •OH.

In addition, ESR spectroscopy (Fig. S22) was performed using DMPO and 2,2,6,6-tetramethylpiperidine (TEMP) as spin trapping agents to further elucidate the presence of •OH, •O₂ and ¹O₂ in all studied systems. Under visible light irradiation, all tested COFs exhibited the signals corresponding to DMPO-•O₂ and TEMP-¹O₂, with the COF-Olefin-2 photocatalytic system demonstrating noticeably stronger signals compared to the other COFs. Specifically, characteristic peaks related to DMPO-•OH were solely evident in the COF-Olefin-2 system. Furthermore, the terephthalic acid-fluorescence (TA-PL) probe (Fig. S23) was also used to determine the cumulative generation of •OH. Notably, upon 40 min of irradiation, the fluorescence intensity near 430 nm of COF-Olefin-2 exhibited a significant increase compared to COF-Olefin-1, while only a marginal enhancement in fluorescence intensity was observed for COF-Olefin-0. These observations suggest that the capacity for •OH production in the COF-Olefin-2 system surpasses that of COF-Olefin-1 and COF-Olefin-0. Quantitative analysis of •OH generation (Fig. S24) further supports this finding, indicating that the COF-Olefin-2 system can yield •OH concentrations of up to 4.17×10^{-15} M at 40 min, exceeding the values obtained for COF-Olefin-1 (3.30×10^{-16} M) and COF-Olefin-0 (1.79×10^{-16} M). Discrepancies between the ESR results and other •OH assay experiments may arise from the brief lifetime of •OH and the DMPO-•OH complex during ESR measurements, rendering it challenging to capture •OH signals accumulated over prolonged periods. It is worth noting that while all three COFs possess the ability to generate •OH, the yields of COF-Olefin-1 and COF-Olefin-0 are

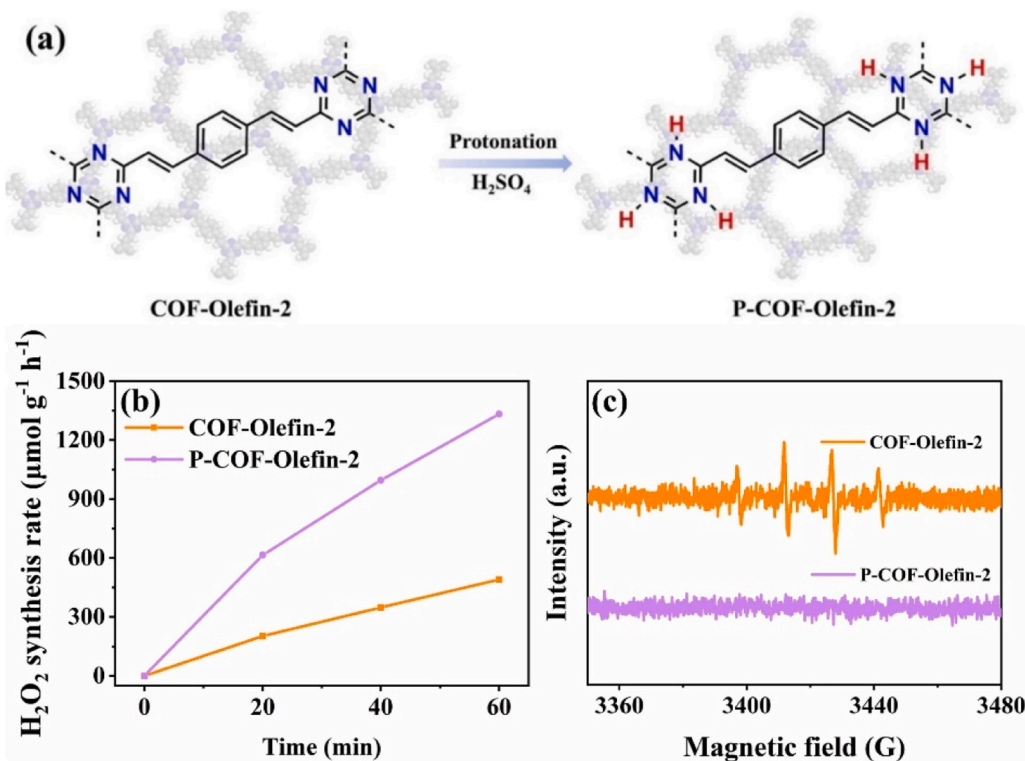


Fig. 5. (a) Synthesis procedure of P-COF-Olefin-2; (b) H₂O₂ synthesis rate of COF-Olefin-2 and P-COF-Olefin-2; (c) ESR spectra of DMPO-•OH in COF-Olefin-2 and P-COF-Olefin-2.

negligible.

The evolution of H₂O₂ were also monitored. As shown in Fig. 3d, COF-Olefin-0 exhibits a minimal H₂O₂ yield of 55 μmol g⁻¹ h⁻¹. Upon introduction of -CH=CH-, the COF-Olefin-1 deliver an enhanced H₂O₂ production rate of 125 μmol g⁻¹ h⁻¹, while COF-Olefin-2, featuring the highest concentration of olefin linkages, displayed a superior yield of 494 μmol g⁻¹ h⁻¹. The remarkable H₂O₂ generation capability of COF-Olefin-2 endows it with greater opportunities for H₂O₂ adsorption and subsequent decomposition into •OH species.

The quenching tests of H₂O₂ production (Fig. 3e and S25) were also conducted to probe the main reactive species responsible for the generation of H₂O₂. Argon (Ar), BQ, EDTA, and potassium bromate (KBrO₃) were utilized to remove O₂, •O₂, h⁺, e⁻, respectively. The results revealed that negligible H₂O₂ was detected after the introduction of Ar, BQ, and KBrO₃, manifesting the production of H₂O₂ occurs through stepwise 1e⁻ ORR. Additionally, based on the generation pathway of H₂O₂ and TA-PL results in Fig. S26, it was observed that there was no fluorescence intensity at 430 nm for COF-Olefin-2 under Ar, indicating that COFs do not generate •OH under Ar. This further confirms that O₂ is necessary for •OH production, and it can be inferred that •OH is generated from H₂O₂ derived from O₂. A two-phase system comprising water and benzyl alcohol (BA) (Fig. 3f) was also established to examine whether decomposition of H₂O₂. In this system, COFs are spontaneously dispersed in the BA phase, while the formed H₂O₂ tend to migrate to the water phase. BA serves as both a phase separation agent and h⁺ scavenger. As a comparison, a water-ethanol system with ethanol as a sacrificial agent (water:ethanol = 9:1) was also employed. After 40 min irradiation, COF-Olefin-2 exhibited an H₂O₂ production rate of 1693 μmol g⁻¹ h⁻¹ in water-BA system, which is 3.38 times than that in water-ethanol system. This indicates that BA plays a more significant role in phase separation compared to its function as a h⁺ scavenger [16, 61]. These findings demonstrate that all three COFs possess the ability to decompose H₂O₂. Notably, COF-Olefin-2 exhibits particularly remarkable H₂O₂ activation ability, as evidenced by its substantial increase in

the water-BA system compared to the other COFs. This characteristic ensures optimal photodegradation performance for COF-Olefin-2.

3.7. Mechanism of •OH production

To gain insight into the atomic-scale mechanism underlying the exceptional ORR performance of COF-Olefin-2, DFT calculations were employed to investigate the O₂ adsorption energy (Fig. 4a, S27, S28, Table S3 and S4) as well as the charge transfer to the O=O bond [62]. Two O₂ adsorption configurations were examined, revealing that the benzene unit exhibited the weakest adsorption energy among all sites, and all sites of COF-Olefin-2 displayed the lowest adsorption energy among all COFs. Furthermore, the charge transfer between O₂ and the catalyst was assessed using Bader analysis. Notably, the O₂ adsorbed on the benzene site of COF-Olefin-2 demonstrated a charge acquisition of 0.231 e⁻, which is significantly higher than that observed for other sites [30,63,64]. These findings indicate that the benzene unit serves as the most active ORR center and that the introduction of -CH=CH- groups enhances the activation of O₂.

Furthermore, the Gibbs free energy of the COFs were simulated to understand the ORR process from a thermodynamic perspective [65]. It is noticeable that when the energy barrier is positive, the reaction cannot proceed spontaneously. As shown in Fig. 4b, the energy barriers of process from O₂ (g) to O₂^{*} for all COFs are positive, indicating that this process is the decisive step for generating H₂O₂. COF-Olefin-2 has the smallest energy barrier (0.65 eV), followed by COF-Olefin-1 (0.98 eV) and the largest by COF-Olefin-0 (0.99 eV) in this process, which suggests that COF-Olefin-2 is more prone to produce H₂O₂, followed by COF-Olefin-1, and finally COF-Olefin-0 [66]. During the process from H₂O₂^{*} to H₂O₂(l), the free energy changes of the three COFs show different trends. The free energies of COF-Olefin-2 and COF-Olefin-1 decreased, indicating that the H₂O₂^{*} can undergo desorption at the benzene site with barrierless, whereas there is an activation energy barrier of 0.08 eV for COF-Olefin-0. The unobstructed

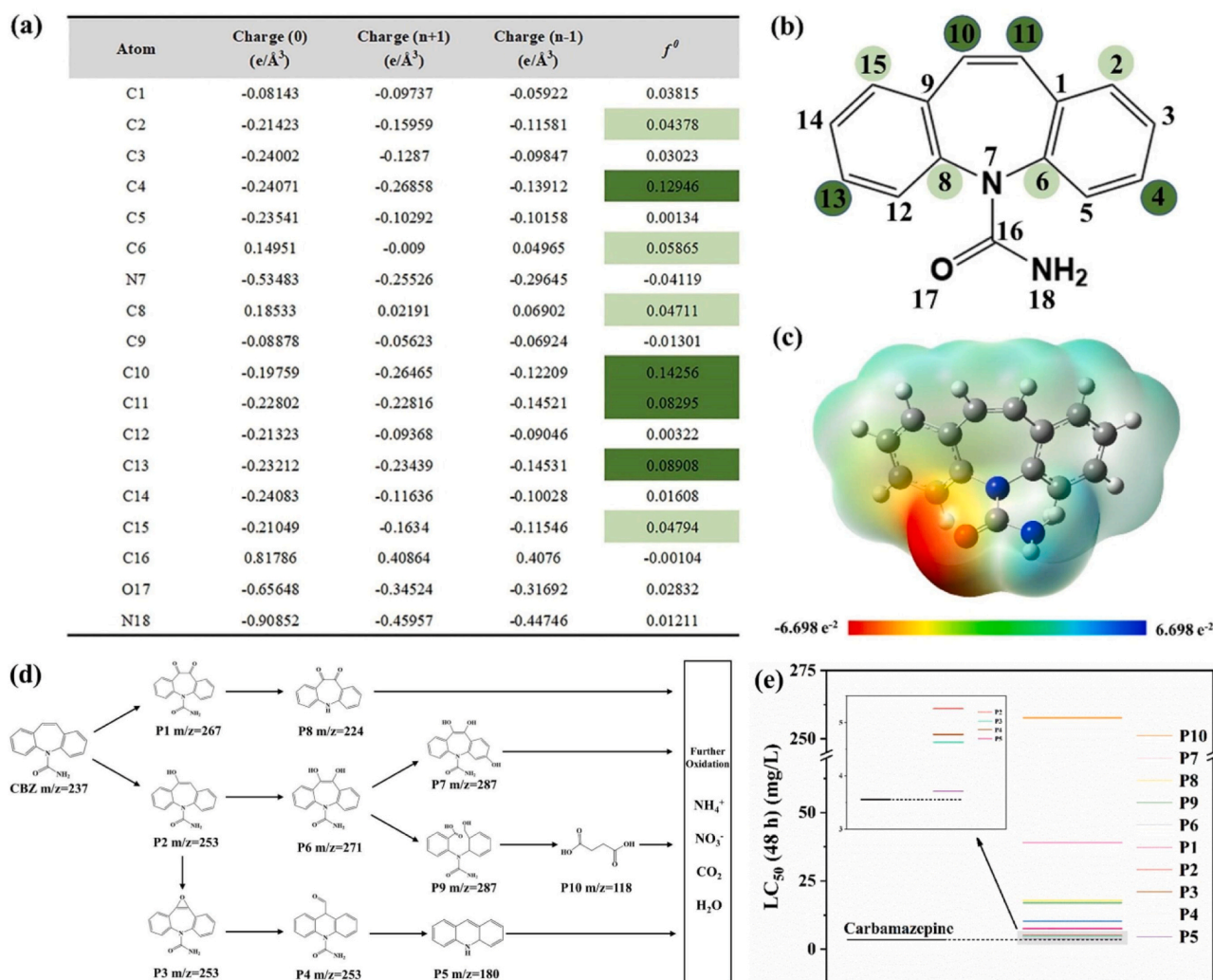


Fig. 6. (a) Natural population analysis (NPA) charge distribution and calculated Fukui Index (f^0) level on CBZ under different electronic states; (b) CBZ molecular structure and corresponding f^0 distribution; (c) Electrostatic potential (ESP) distribution of CBZ; (d) Proposed photocatalytic degradation pathways of CBZ and (e) Mutagenicity of CBZ and intermediates in the COF-Olefin-2 system (taking *Daphnia magna* as an example).

desorption of H_2O_2^* suggests that H_2O_2 is not prone to *in situ* decomposition, but the decomposition experiments of H_2O_2 show that all three COFs are decomposed to a certain extent, especially COF-Olefin-2. Therefore, H_2O_2 adsorbed again to the surface of the COFs after desorption. In order to accurately locate the activation site of H_2O_2 on COF, we performed calculations related to the adsorption of H_2O_2 . In Fig. 4c, when H_2O_2 is adsorbed at the triazine site, a large number of electron migration activities exist in the COF and H_2O_2 , and the O—O bond of H_2O_2 acquires $1.23 e^-$ and the maximum O—O single bond stretch (1.48 \AA). Although O—O bond at benzene site also obtains large e^- and elongating, quite weak adsorption energy result in feebly activate H_2O_2 . With the increasing number of $-\text{C}=\text{C}-$, the activation energy barrier of H_2O_2 to $\bullet\text{OH}$ gradually decreases, and both COF-Olefin-2 (-0.12 eV) and COF-Olefin-1 (-0.03 eV) can be elongated barrierless (Fig. 4d) [67]. In summary, the increase of olefinic π -bridges facilitated electron transfer within the framework of COFs and connected the ORR and H_2O_2 adsorption-decomposition site, enabling the decomposition of H_2O_2 adsorbed at the triazine site to produce $\bullet\text{OH}$ (Fig. 4e). After the triazine of COF was protonated (P-COF-Olefin-2), the H_2O_2 production increased significantly and the DMPO- $\bullet\text{OH}$ signal disappeared (Fig. 5). Those may be caused by the absence of triazine site so that H_2O_2 could not be activated, which also confirmed that the triazine site played a role in activating H_2O_2 to $\bullet\text{OH}$. Considering the possibility of h^+ oxidizing H_2O_2 to $\bullet\text{OH}$, TA-PL probe experiments were also conducted after

capturing h^+ (Fig. S29). The results showed that the fluorescence intensity did not change significantly after the capture of h^+ , indicating that h^+ was not involved in the process of converting H_2O_2 to $\bullet\text{OH}$. In order to further verify the role of h^+ in the reaction process, dissolved O_2 detection experiments were conducted. From Fig. S30, it can be seen that the dissolved O_2 in the COF-Olefin-2 system increases with the prolongation of irradiation time, indicating that the main role of h^+ is to oxidize H_2O to generate O_2 (Eq. (4)).



In addition, the DO test for COF-Olefin-1 and COF-Olefin-0 was also conducted in the system without O_2 (Fig. S31). The obvious O_2 signal in all COFs was detected during the whole reaction period, demonstrating all COFs can achieve saturation in O_2 adsorption solely relying on the O_2 produced through the oxidation of H_2O . Achieving O_2 adsorption saturation is easier in an open system. However, it is worth noting that the O_2 adsorption sites in the COFs are located in the benzene units rather than the $-\text{C}=\text{C}-$ groups, which are responsible for increasing the pore size. Therefore, the increased pore size resulting from the introduction of $-\text{C}=\text{C}-$ groups does not lead to an increase in O_2 adsorption sites. This implies that the pore width does not significantly influence the photocatalytic performance of the COFs.

3.8. Degradation pathway analysis

To further explore the degradation pathway, the Fukui Index (f^0) was calculated through natural population analysis (NPA) charge to predict the radical-related CBZ degradation process. The NPA charge distribution for 0, +1 and -1 are shown in Fig. 6a and the $\bullet\text{O}_2$ and $\bullet\text{OH}$ tend to attack the sites with higher f^0 values. Fig. 6b displays the most reactive sites, which are C10 (0.14256), C4 (0.12946), C13 (0.08908) and C11 (0.08295), separately. Considering C4 and C13 are located on the benzene site, which is more difficult to react, these sites are generally not considered. The electrostatic surface potential (ESP) diagram in Fig. 6c represents the distribution of electron clouds in CBZ, where the red and blue regions represent the electron-rich and electron-deficient areas of CBZ molecules, respectively, and due to electrostatic attraction, the electron-deficient region is susceptible to $\bullet\text{O}_2$ and $\bullet\text{OH}$ attack [68]. Thus, C10 and C11 are extremely susceptible to the influence of radicals in the COF-Olefin-2 system.

The degradation intermediates during the reaction were investigated by liquid chromatograph mass spectrometer (LC-MS) to further understand the degradation pathways of CBZ and ten main degradation intermediates were detected (Fig. S32). Combining the f^0 , ESP results and the analysis of ROSSs, the proposed photocatalytic degradation pathways of CBZ were presented in Fig. 6d. The characteristic peak of the original CBZ molecule located at $m/z = 237$, and then $\bullet\text{O}_2$ and $\bullet\text{OH}$ preferred to attack the C10 and C11 sites to form P1 ($m/z = 267$) and P2 ($m/z = 253$), and $^1\text{O}_2$ also involved. P1 ($m/z = 267$) was oxidized by ROSSs and lost its amide group to form P8 ($m/z = 224$). P2 ($m/z = 253$) underwent a continuous aromatic ring hydroxylation reaction under the continuous attack of $\bullet\text{OH}$, forming P6 ($m/z = 271$) and P7 ($m/z = 287$) in sequence. Continuous hydroxylation also promotes the occurrence of ring-opening reactions, P9 ($m/z = 287$) and P10 ($m/z = 118$) are products of the ring-opening reaction under the action of ROSSs. In addition, P2 ($m/z = 253$) was also attacked by $\bullet\text{OH}$, forming a hydroxylated product P3 ($m/z = 253$), which then destroyed the heptatomic ring. However, the generated intermediate suffered from the ring contraction to form P4 ($m/z = 253$) due to instability. Further conversion of P4 ($m/z = 253$) led to aldehyde and amide group cleavage to form P5 ($m/z = 180$) [69–71]. The toxicity of degradation intermediates (*Daphnia magna* LC_{50} , 48 h) (Fig. 6e) was predicted by T.E.S.T. software [72]. The predicted LC_{50} value of CBZ was 3.56 mg L^{-1} , and the value of all intermediates are greater than CBZ, which indicates that the toxicity of intermediates has decreased with the progress of photocatalytic degradation process.

4. Conclusions

In conclusion, COF-Olefin-0, COF-Olefin-1, and COF-Olefin-2 were successfully synthesized to probe the structure-function relationship towards efficient $\bullet\text{OH}$ production via CB-e⁻. Experimental investigations and DFT calculations revealed that the incorporation of -CH=CH- not only enhances the carrier migration efficiency of COFs through increased π -conjugation but also achieves spatial separation of benzene-triazine dual sites. These characteristics optimize the $\bullet\text{OH}$ generation pathway, leading to remarkable solar-driven H_2O_2 production and subsequently to H_2O_2 -to- $\bullet\text{OH}$ conversion at lower oxidation potentials. Consequently, this optimized process demonstrated exceptional efficacy in the photodegradation of PPCPs. Importantly, these findings offer valuable insights into the design and fabrication of high-performance COFs and the fine-tuning of the $\bullet\text{OH}$ generation pathway, with promising applications in utilizing solar energy for water environment purification.

CRediT authorship contribution statement

Jinhong Bi: Writing – review & editing, Supervision, Funding acquisition. **Liuyi Li:** Writing – review & editing, Investigation. **Ling Wu:** Investigation, Formal analysis. **Qiaoshan Chen:** Investigation,

Formal analysis. **Guocheng Huang:** Writing – review & editing, Supervision, Methodology. **Jinpeng Zhang:** Writing – original draft, Methodology, Formal analysis, Conceptualization.

Declaration of Competing Interest

The authors declare that they have no known competing financial interests or personal relationships that could have appeared to influence the work reported in this paper.

Data availability

Data will be made available on request.

Acknowledgment

This work was financially supported by the National Natural Science Foundation of China (22272028, 21707173), the Youth Talent Support Program of Fujian Province (00387077), the National Natural Science Foundation of Fujian Province (2022J01110), the Joint Funds of Tianjin University and Fuzhou University (00388036).

Appendix A. Supporting information

Supplementary data associated with this article can be found in the online version at doi:10.1016/j.apcatb.2024.124216.

References

- [1] S. Luo, L. Gao, Z. Wei, R. Spinney, D.D. Dionysiou, W.-P. Hu, L. Chai, R. Xiao, Kinetic and mechanistic aspects of hydroxyl radical-mediated degradation of naproxen and reaction intermediates, *Water Res.* 137 (2018) 233–241.
- [2] W.-C. Huang, M. Liu, F.-G. Zhang, D. Li, Y. Du, Y. Chen, Q.-Y. Wu, Removal of disinfection byproducts and toxicity of chlorinated water by post-treatments of ultraviolet/hydrogen peroxide and ultraviolet/peroxymonosulfate, *J. Clean. Prod.* 352 (2022) 131563.
- [3] M. Chen, L. Ding, S. Zhu, X. Xiong, X. Yuan, Y. Peng, L. Yang, H. Shi, P. Shao, X. Luo, Decomplexation of Ni-EDTA enhanced by Fe(III) reduction in the fenton reaction: insight into the role of carbonyl groups, *J. Environ. Chem. Eng.* 11 (2023) 111097.
- [4] G. Liu, J. Ji, H. Huang, R. Xie, Q. Feng, Y. Shu, Y. Zhan, R. Fang, M. He, S. Liu, X. Ye, D.Y.C. Leung, UV/ H_2O_2 : an efficient aqueous advanced oxidation process for VOCs removal, *Chem. Eng. J.* 324 (2017) 44–50.
- [5] W. Wang, W. Gu, G. Li, H. Xie, P.K. Wong, T. An, Few-layered tungsten selenide as a co-catalyst for visible-light-driven photocatalytic production of hydrogen peroxide for bacterial inactivation, *Environ. Sci. Nano* 7 (2020) 3877–3887.
- [6] T. Liu, L. Wang, C. Sun, X. Liu, R. Miao, Y. Lv, A comparison of the photolytic and photocatalytic degradation of fluvastatin, *Chem. Eng. J.* 358 (2019) 1296–1304.
- [7] S. Shu, H. Wang, X. Guo, Y. Wang, X. Zeng, Efficient photocatalytic degradation of sulfamethazine by Cu-Cu₂O/TiO₂ composites: performance, photocatalytic mechanism and degradation pathways, *Sep. Purif. Technol.* 323 (2023) 124458.
- [8] X. Zeng, S. Shu, Y. Meng, H. Wang, Y. Wang, Enhanced photocatalytic degradation of sulfamethazine by g-C₃N₄/Cu, N-TiO₂ composites under simulated sunlight irradiation, *Chem. Eng. J.* 456 (2023) 141105.
- [9] J. Kim, C.W. Lee, W. Choi, Platinized WO₃ as an environmental photocatalyst that generates OH radicals under visible light, *Environ. Sci. Technol.* 44 (2010) 6849–6854.
- [10] L. Su, P. Wang, X. Ma, J. Wang, S. Zhan, Regulating local electron density of iron single sites by introducing nitrogen vacancies for efficient photo-fenton process, *Angew. Chem. Int. Ed.* 60 (2021) 21261–21266.
- [11] J. Zhang, C. Yu, J. Lang, Y. Zhou, B. Zhou, Y.H. Hu, M. Long, Modulation of Lewis acidic-basic sites for efficient photocatalytic H_2O_2 production over potassium intercalated tri-s-triazine materials, *Appl. Catal. B Environ.* 277 (2020) 119225.
- [12] J. Ye, A. Hu, C. Gao, F. Li, L. Li, Y. Guo, G. Ren, B. Li, C. Rensing, K.H. Nealon, S. Zhou, Y. Xiong, Abiotic methane production driven by ubiquitous non-fenton-type reactive oxygen species, *Angew. Chem. Int. Ed.* 63 (2024) e202403884.
- [13] Y. Hong, Y. Cho, E.M. Go, P. Sharma, H. Cho, B. Lee, S.M. Lee, S.O. Park, M. Ko, S. K. Kwak, C. Yang, J.-W. Jang, Unassisted photocatalytic H_2O_2 production under visible light by fluorinated polymer-TiO₂ heterojunction, *Chem. Eng. J.* 418 (2021) 129346.
- [14] A. Bard, *Standard Potentials in Aqueous Solution*, Routledge, 2017.
- [15] Y. Nosaka, A.Y. Nosaka, Generation and detection of reactive oxygen species in photocatalysis, *Chem. Rev.* 117 (2017) 11302–11336.
- [16] J. Sun, H. Sekhar Jena, C. Krishnaraj, K. Singh Rawat, S. Abednatanzi, J. Chakraborty, A. Laemont, W. Liu, H. Chen, Y.-Y. Liu, K. Leus, H. Vrielinck, V. Van Speybroeck, P. Van Der Voort, Pyrene-based covalent organic frameworks

- for photocatalytic hydrogen peroxide production, *Angew. Chem. Int. Ed.* 62 (2023) e202216719.
- [17] Q. Niu, L. Mi, W. Chen, Q. Li, S. Zhong, Y. Yu, L. Li, Review of covalent organic frameworks for single-site photocatalysis and electrocatalysis, *Chin. J. Catal.* 50 (2023) 45–82.
 - [18] Y. Liu, W.-K. Han, W. Chi, J.-X. Fu, Y. Mao, X. Yan, J.-X. Shao, Y. Jiang, Z.-G. Gu, One-dimensional covalent organic frameworks with atmospheric water harvesting for photocatalytic hydrogen evolution from water vapor, *Appl. Catal. B Environ.* 338 (2023) 123074.
 - [19] P. Das, J. Roeser, A. Thomas, Solar light driven H_2O_2 production and selective oxidations using a covalent organic framework photocatalyst prepared by a multicomponent reaction, *Angew. Chem. Int. Ed.* 62 (2023) e202304349.
 - [20] J.-Y. Yue, L.-P. Song, Y.-F. Fan, Z.-X. Pan, P. Yang, Y. Ma, Q. Xu, B. Tang, Thiophene-containing covalent organic frameworks for overall photocatalytic H_2O_2 synthesis in water and seawater, *Angew. Chem. Int. Ed.* 62 (2023) e202309624.
 - [21] S. Zhang, W. Huang, P. Hu, C. Huang, C. Shang, C. Zhang, R. Yang, G. Cui, Conjugated microporous polymers with excellent electrochemical performance for lithium and sodium storage, *J. Mater. Chem. A* 3 (2015) 1896–1901.
 - [22] F. Jiang, Y. Wang, T. Qiu, G. Yang, C. Yang, J. Huang, Z. Fang, J. Li, Synthesis of biphenyl-linked covalent triazine frameworks with excellent lithium storage performance as anode in lithium ion battery, *J. Power Sources* 523 (2022) 231041.
 - [23] C. Krishnaraj, H. Sekhar Jena, L. Bourda, A. Laemont, P. Pachfule, J. Roeser, C. V. Chandran, S. Borgmans, S.M.J. Rogge, K. Leus, C.V. Stevens, J.A. Martens, V. Van Speybroeck, E. Breynaert, A. Thomas, P. Van Der Voort, Strongly reducing (diarylamino)benzene-based covalent organic framework for metal-free visible light photocatalytic H_2O_2 generation, *J. Am. Chem. Soc.* 142 (2020) 20107–20116.
 - [24] Q. Liao, D. Wang, C. Ke, Y. Zhang, Q. Han, Y. Zhang, K. Xi, Metal-free fenton-like photocatalysts based on covalent organic frameworks, *Appl. Catal. B Environ.* 298 (2021) 120548.
 - [25] H. Li, H. Li, S. Xun, J.-L. Brédas, Doping modulation of the charge injection barrier between a covalent organic framework monolayer and graphene, *Chem. Mater.* 32 (2020) 9228–9237.
 - [26] L. Jin, M. Sun, J. Yang, Y. Huang, Y. Liu, Janus photoelectrocatalytic filter for sustainable water decontamination, *Appl. Catal. B Environ.* 339 (2023) 123150.
 - [27] L. Peng, S. Chang, Z. Liu, Y. Fu, R. Ma, X. Lu, F. Zhang, W. Zhu, L. Kong, M. Fan, Visible-light-driven photocatalytic CO_2 reduction over ketoenamine-based covalent organic frameworks: role of the host functional groups, *Catal. Sci. Technol.* 11 (2021) 1717–1724.
 - [28] C. Yang, C. Qian, M. Yu, Y. Liao, Manipulation of band gap and hydrophilicity in vinylene-linked covalent organic frameworks for improved visible-light-driven hydrogen evolution by end-capping strategy, *Chem. Eng. J.* 454 (2023) 140341.
 - [29] L. Sun, L. Li, J. Yang, J. Fan, Q. Xu, Fabricating covalent organic framework/CdS S-scheme heterojunctions for improved solar hydrogen generation, *Chin. J. Catal.* 43 (2022) 350–358.
 - [30] H. Chen, S. Gao, G. Huang, Q. Chen, Y. Gao, J. Bi, Built-in electric field mediated S-scheme charge migration in COF/ In_2S_3 heterojunction for boosting H_2O_2 photosynthesis and sterilization, *Appl. Catal. B Environ.* 343 (2024) 123545.
 - [31] C. Qin, X. Wu, L. Tang, X. Chen, M. Li, Y. Mou, B. Su, S. Wang, C. Feng, J. Liu, X. Yuan, Y. Zhao, H. Wang, Dual donor-acceptor covalent organic frameworks for hydrogen peroxide photosynthesis, *Nat. Commun.* 14 (2023) 5238.
 - [32] Y. Qian, Y. Han, X. Zhang, G. Yang, G. Zhang, H.-L. Jiang, Computation-based regulation of excitonic effects in donor-acceptor covalent organic frameworks for enhanced photocatalysis, *Nat. Commun.* 14 (2023) 3083.
 - [33] T. Jadhav, Y. Fang, W. Patterson, C.-H. Liu, E. Hamzehpoor, D.F. Perepichka, 2D poly(arylene vinylene) covalent organic frameworks via aldol condensation of trimethyltriazine, *Angew. Chem. Int. Ed.* 58 (2019) 13753–13757.
 - [34] J. Xu, Y. He, S. Bi, M. Wang, P. Yang, D. Wu, J. Wang, F. Zhang, An olefin-linked covalent organic framework as a flexible thin-film electrode for a high-performance micro-supercapacitor, *Angew. Chem. Int. Ed.* 58 (2019) 12065–12069.
 - [35] T. He, K. Geng, D. Jiang, All sp^2 carbon covalent organic frameworks, *Trends Chem.* 3 (2021) 431–444.
 - [36] F. Zhang, H. Hao, X. Dong, X. Li, X. Lang, Olefin-linked covalent organic framework nanotubes based on triazine for selective oxidation of sulfides with O_2 powered by blue light, *Appl. Catal. B Environ.* 305 (2022) 121027.
 - [37] L. Zhai, S. Yang, X. Yang, W. Ye, J. Wang, W. Chen, Y. Guo, L. Mi, Z. Wu, C. Soutis, Q. Xu, Z. Jiang, Conjugated covalent organic frameworks as platinum nanoparticle supports for catalyzing the oxygen reduction reaction, *Chem. Mater.* 32 (2020) 9747–9752.
 - [38] S. Wei, F. Zhang, W. Zhang, P. Qiang, K. Yu, X. Fu, D. Wu, S. Bi, F. Zhang, Semiconducting 2D triazine-cored covalent organic frameworks with unsubstituted olefin linkages, *J. Am. Chem. Soc.* 141 (2019) 14272–14279.
 - [39] R.-H. Xu, W.-R. Cui, C.-R. Zhang, X.-R. Chen, W. Jiang, R.-P. Liang, J.-D. Qiu, Vinylene-linked covalent organic frameworks with enhanced uranium adsorption through three synergistic mechanisms, *Chem. Eng. J.* 419 (2021) 129550.
 - [40] G. Yang, R. Wang, D. Fang, T. Hu, C. Bao, J. Yi, Nano-silver modified carbon nanotubes to reinforce the copper matrix composites and their mechanical properties, *Adv. Powder Technol.* 33 (2022) 103672.
 - [41] K. Xiong, Y. Wang, F. Zhang, X. Li, X. Lang, Linker length-dependent photocatalytic activity of β -ketoenamine covalent organic frameworks, *Appl. Catal. B Environ.* 322 (2023) 122135.
 - [42] Y. Zheng, S. Chen, K.A.I. Zhang, J. Zhu, J. Xu, C. Zhang, T. Liu, Ultrasound-triggered assembly of covalent triazine framework for synthesizing heteroatom-doped carbon nanoflowers boosting metal-free bifunctional electrocatalysis, *ACS Appl. Mater. Interfaces* 13 (2021) 13328–13337.
 - [43] X. Dong, F. Huang, Y. Wang, K. Zhang, X. Lang, Selective oxidation of sulfides by pyrene- π -anthraquinone conjugated microporous polymer photocatalysis, *Mater. Today Energy* 38 (2023) 101443.
 - [44] Z. Li, X. Chen, G. Huang, J. Wang, Y.-T. Sham, M. Pan, J. Bi, Highly porous NiFe-mixed metal oxides derived from calcinated layered double hydroxide for efficient antibiotics removal, *Appl. Surf. Sci.* 644 (2024) 158728.
 - [45] F. Zhang, S. Wei, W. Wei, J. Zou, G. Gu, D. Wu, S. Bi, F. Zhang, Trimethyltriazine-derived olefin-linked covalent organic framework with ultralong nanofibers, *Sci. Bull.* 65 (2020) 1659–1666.
 - [46] M. Liu, Q. Huang, S. Wang, Z. Li, B. Li, S. Jin, B. Tan, Crystalline covalent triazine frameworks by *in situ* oxidation of alcohols to aldehyde monomers, *Angew. Chem. Int. Ed.* 57 (2018) 11968–11972.
 - [47] J. Bi, Z. Zhang, J. Tian, G. Huang, Interface engineering in a nitrogen-rich COF/BiOBr S-scheme heterojunction triggering efficient photocatalytic degradation of tetracycline antibiotics, *J. Colloid Interface Sci.* 661 (2024) 761–771.
 - [48] X. Li, B. Kang, F. Dong, Z. Zhang, X. Luo, L. Han, J. Huang, Z. Feng, Z. Chen, J. Xu, B. Peng, Z.L. Wang, Enhanced photocatalytic degradation and H_2/H_2O_2 production performance of S-pCN/ $WO_{2.72}$ S-scheme heterojunction with appropriate surface oxygen vacancies, *Nano Energy* 81 (2021) 105671.
 - [49] Z. Hu, L. Yuan, Z. Liu, Z. Shen, J.C. Yu, An elemental phosphorus photocatalyst with a record high hydrogen evolution efficiency, *Angew. Chem. Int. Ed.* 55 (2016) 9580–9585.
 - [50] Y. Deng, M. Batmunkh, L. Ye, C. Song, T. Ge, Y. Xu, X. Mu, W. Liu, X. Jin, P. K. Wong, H. Huang, Q. Wang, X. Zhuang, T. Ma, Integrated full-spectrum solar energy catalysis for zero-emission ethylene production from bioethanol, *Adv. Funct. Mater.* 32 (2022) 2110026.
 - [51] F. Chen, Z. Ma, L. Ye, T. Ma, T. Zhang, Y. Zhang, H. Huang, Macroscopic spontaneous polarization and surface oxygen vacancies collaboratively boosting CO_2 photoreduction on BiOI/ Fe_2O_3 single crystals, *Adv. Mater.* 32 (2020) 1908350.
 - [52] H. Li, Y. Chen, Q. Niu, X. Wang, Z. Liu, J. Bi, Y. Yu, L. Li, The crystalline linear polyimide with oriented photogenerated electron delivery powering CO_2 reduction, *Chin. J. Catal.* 49 (2023) 152–159.
 - [53] Y. Yang, N. Luo, S. Lin, H. Yao, Y. Cai, Cyano substituent on the olefin linkage: promoting rather than inhibiting the performance of covalent organic frameworks, *ACS Catal.* 12 (2022) 10718–10726.
 - [54] F. Tian, X. Huang, W. Li, Y. An, G. Li, R. Chen, Weak interaction between nickel thiolate and $g-C_3N_4$ improving electron-hole separation for photocatalysis, *ACS Catal.* 13 (2023) 12186–12196.
 - [55] B. Mourino, K.M. Jablonka, A. Ortega-Guerrero, B. Smit, In search of covalent organic framework photocatalysts: a DFT-based screening approach, *Adv. Funct. Mater.* 33 (2023) 2301594.
 - [56] Z. Zhao, X. Chen, B. Li, S. Zhao, L. Niu, Z. Zhang, Y. Chen, Spatial regulation of acceptor units in olefin-linked COFs toward highly efficient photocatalytic H_2 evolution, *Adv. Sci.* 9 (2022) 2203832.
 - [57] J.-X. Tan, Z.-Y. Chen, C.H. Chen, M.-F. Hsieh, A.Y.-C. Lin, S.S. Chen, K.C.W. Wu, Efficient adsorption and photocatalytic degradation of water emerging contaminants through nanoarchitectonics of pore sizes and optical properties of zirconium-based MOFs, *J. Hazard. Mater.* 451 (2023) 131113.
 - [58] D. Li, P. Yu, X. Zhou, J.-H. Kim, Y. Zhang, P.J.J. Alvarez, Hierarchical Bi_2O_3/CO_3 wrapped with modified graphene oxide for adsorption-enhanced photocatalytic inactivation of antibiotic resistant bacteria and resistance genes, *Water Res.* 184 (2020) 116157.
 - [59] J. Ye, Y. Chen, C. Gao, C. Wang, A. Hu, G. Dong, Z. Chen, S. Zhou, Y. Xiong, Sustainable conversion of microplastics to methane with ultrahigh selectivity by a biotic–abiotic hybrid photocatalytic system, *Angew. Chem. Int. Ed.* 61 (2022) e202213244.
 - [60] Q. Chen, H. Zhou, J. Wang, J. Bi, F. Dong, Activating earth-abundant insulator $BaSO_4$ for visible-light induced degradation of tetracycline, *Appl. Catal. B Environ.* 307 (2022) 121182.
 - [61] X. Li, C. Chen, J. Zhao, Mechanism of photodecomposition of H_2O_2 on TiO_2 surfaces under visible light irradiation, *Langmuir* 17 (2001) 4118–4122.
 - [62] K.-Y. Chen, Y.-X. Huang, R.-C. Jin, B.-C. Huang, Single atom catalysts for use in the selective production of hydrogen peroxide via two-electron oxygen reduction reaction: mechanism, activity, and structure optimization, *Appl. Catal. B Environ.* 337 (2023) 122987.
 - [63] Y. He, J. Zhao, Y.-T. Sham, S. Gao, M. Pan, Q. Chen, G. Huang, P.K. Wong, J. Bi, Efficient hydrogen peroxide photosynthesis over CdS/COF for water disinfection: the S-scheme pathway, oxygen adsorption, and reactor design, *ACS Sustain. Chem. Eng.* 11 (2023) 17552–17563.
 - [64] P. Hu, G. Liang, B. Zhu, W. Macyk, J. Yu, F. Xu, Highly selective photoconversion of CO_2 to CH_4 over $SnO_2/Cs_3Bi_2Br_9$ heterojunctions assisted by S-scheme charge separation, *ACS Catal.* 13 (2023) 12623–12633.
 - [65] Z. Weng, Y. Lin, S. Guo, X. Zhang, Q. Guo, Y. Luo, X. Ou, J. Ma, Y. Zhou, J. Jiang, B. Han, Site Engineering of covalent organic frameworks for regulating peroxymonosulfate activation to generate singlet oxygen with 100 % selectivity, *Angew. Chem. Int. Ed.* 62 (2023) e202310934.
 - [66] L. Wang, J. Zhang, Y. Zhang, H. Yu, Y. Qu, J. Yu, Inorganic metal-oxide photocatalyst for H_2O_2 production, *Small* 18 (2022) 2104561.
 - [67] C. Ling, X. Liu, H. Li, X. Wang, H. Gu, K. Wei, M. Li, Y. Shi, H. Ben, G. Zhan, C. Liang, W. Shen, Y. Li, J. Zhao, L. Zhang, Atomic-layered Cu_5 nanoclusters on FeS_2 with dual catalytic sites for efficient and selective H_2O_2 activation, *Angew. Chem. Int. Ed.* 61 (2022) e202200670.
 - [68] D. Zhang, Y. Liu, Y. Song, X. Sun, W. Liu, J. Duan, Z. Cai, Synergistic effect of Fe and Ce on Fe doped CeO_2 for catalytic ozonation of amoxicillin: efficiency evaluation and mechanism study, *Sep. Purif. Technol.* 313 (2023) 123430.

- [69] S. Wang, J. Wang, Degradation of carbamazepine by radiation-induced activation of peroxymonosulfate, *Chem. Eng. J.* 336 (2018) 595–601.
- [70] Y. Hong, H. Zhou, Z. Xiong, Y. Liu, G. Yao, B. Lai, Heterogeneous activation of peroxymonosulfate by CoMgFe-LDO for degradation of carbamazepine: efficiency, mechanism and degradation pathways, *Chem. Eng. J.* 391 (2020) 123604.
- [71] J. Zhai, Q. Wang, Q. Li, B. Shang, M.H. Rahaman, J. Liang, J. Ji, W. Liu, Degradation mechanisms of carbamazepine by δ -MnO₂: role of protonation of degradation intermediates, *Sci. Total Environ.* 640-641 (2018) 981–988.
- [72] W. Zhao, M. Yan, Y. Chen, J. Shen, X. Hong, F. Mu, S. Li, S. Zhang, Q. Wang, B. Dai, Y. Liu, C. Sun, Rational design of novel metal-organic framework/Bi₄O₇ S-scheme heterojunction photocatalyst for boosting carbamazepine degradation, *Appl. Surf. Sci.* 622 (2023) 156876.